Chapter 5

Tuning of Redox Energy of Transition - Metal Ions through the Utilization of Interlayer Potentials in Layered Perovskites: Development of a Titanium - Based Superior HER catalyst in Acidic Medium

5.1. Introduction

With the excessive usage of fossil fuels, the natural resources of fossil fuels are exhausting at an alarming rate, also causing a detrimental impact on the environment. Non-conventional energy (renewable energy) resources coupled with a hydrogen economy are considered the light for the future to make a safer and better world. [1-4] Hydrogen energy, which exploits safe, clean and sustainable energy sources, can become an alternative as a clean fuel (is considered a potential energy resource). [5-7] Efficient electrolysis of water is important for hydrogen production, [8-9] which uses efficient catalysts having active sites for the hydrogen evolution reaction to reduce the electrode overpotential. [9-14] Molecular hydrogen as an energy carrier is advantageous because H_2 is with the highest energy density per unit mass, H_2O is the only by-product when H_2 is transformed into electricity in a solid oxide fuel cell or combusted in an engine. [15-17]

Electrochemical water splitting was the very first time observed in 1789 and the process involve two half-cell reactions i.e., hydrogen evolution reaction (HER) and oxygen evolution reaction (OER). [18] Most efficient HER catalysts are Pt, Ru and Ir-based noble metals, which catalyze HER with near-zero overpotential. However, the high cost and scarcity of these materials limit their large-scale applications. [19-20] In the past few decades, investigating water catalyzers with different combinations of materials, including metals, metal alloys, [21] metals modified with transition-metal carbides, [22] phosphides, [23] nitrides, [24] chalcogenides, [25] heteroatom doped carbon nanostructures [26-27] and transition metal compounds [28-29] that have been used for the efficient conversion of H_3O^+ (acidic) and H_2O (alkaline) to molecular hydrogen.

Among many candidates, inorganic materials belonging to the perovskite family, Ruddlesden–Popper (RP) type layered perovskites, have been intensively studied as electrocatalysts for HER and OER. Very recently, RP-phase type layered perovskites (general

formula: $A_{n+1}B_nX_{3n+1}$ or $AX(ABX_3)_n$ (n = 1, 2, 3 or more), containing alternating rock-salt layers (AX) and perovskite-like layers (ABX_3) along the crystallographic *c*-axis have emerged as a new class of water-splitting electrocatalysts. [30, 31] Among these, Sr_2RuO_4 showed remarkable HER activity comparable to the commercial Pt/C catalyst. Besides, due to the layered structure and unique structural properties, RP-phase layered perovskite also finds applications as electrocatalysts for catalyzing a variety of chemical reactions, including the oxygen (O_2) reduction/evolution, [32] H_2 evolution, nitrogen reduction, CO_2 conversion, hydrogen peroxide (H_2O_2) reduction and urea/methanol/ethanol oxidation for low-temperature electrolysis cells, fuel cells, and metal–air batteries. [33,34] Electrocatalysis utilizes the active redox couple of the active cations in the framework; the host cations accept/donate electrons for each such electrochemical conversion reaction. [35] The redox energies of transition-metal cations in oxides vary with the crystal structure of the oxide and any counter-cation present in the lattice. The relative position of these redox energies with respect to Fermi level and controlling their variations in different oxides are important for the designing novel electrocatalyst and electrodes for electrochemical cells such as batteries, pseudocapacitors as well as heterogeneous catalysts and photocatalysts, also important for altering the electrical, electronic and magnetic properties of electronic materials. [36-37]

In layered perovskite (RP-phase perovskites phase; $A_{n+1}B_nX_{3n+1,}$ n=1; A_2BX_4) structures, especially in the form of AA`BO_4 structure, the redox energies of B cation can be tuned by controlling the counter-cationic interaction in alternating layers. Structure of layered perovskite, $NaYTiO_4$ can be visualized as TiO_6 octahedra separated by alternating Na^+–O^{2-} and Y^{3+}-O^{2-} layers and relative charges on individual layers can impose a dipolar electric field that is termed as interlayer potential on TiO_6 octahedra that not only result in distortion/elongation of TiO_6

octahedra as represented in **Figure 5.1** but also alter the relative band position and redox energy of active $Ti^{4+/3+}$ redox couple.

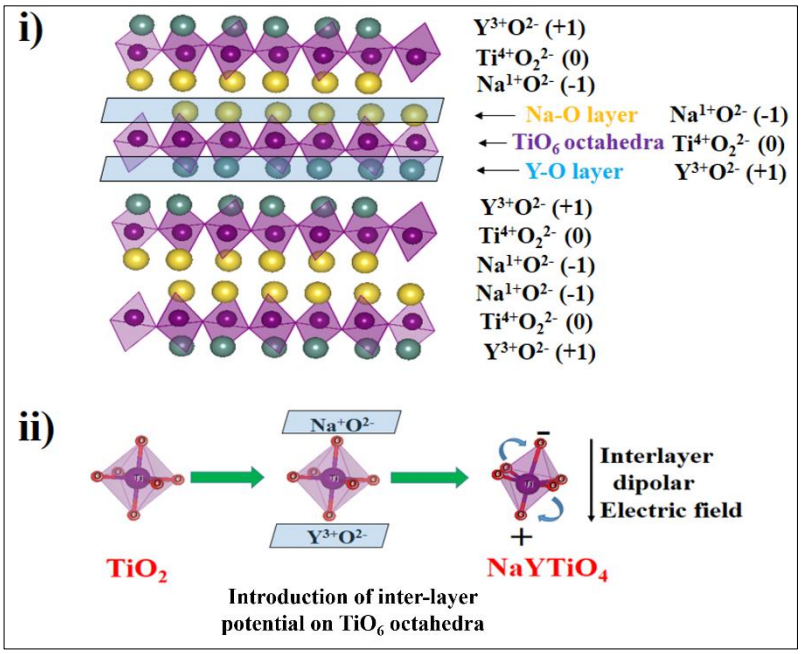

Figure 5.1. (i) Depicting the interlayer potential on TiO_6 octahedra or TiO_2 layer & **(ii)** Distortion in TiO_6 octahedra due to interlayer potential.

Interaction between the different charge layers (Na^{+}-O^{2-} and Y^{3+}-O^{2-}) over TiO_6 octahedra, the interlayer dipolar electric field is envisaged here as the inter-layer potential that can be varied to tune the redox energies and relative redox position of $Ti^{4+/3+}$ redox couple with respect to Fermi level to develop superior electrocatalyst for HER and can act as a controlling force to direct the electronic interaction and electron transfer rates in electrocatalytic reactions.

In this chapter, we report the usage of this inter-layer potential to tune the relative redox energies of the Ti(IV)/Ti(III) redox couples in layered titanates $NaYTiO_4$ by doping of different cations in the rock-salt layer. The interlayer internal electric field (interlayer potential) perpendicular to the layers containing TiO_6 octahedra to tune the Ti(IV)/Ti(III) redox energy and the relative position of the Ti(IV)/Ti(III) redox couple is utilized here to develop a superior HER electrocatalyst. Here, we report $NaYTiO_4$ as a model host lattice to study the relative position of the Ti(IV)/Ti(III) redox couple compared to that in the TiO_2 for accessing superior electrocatalytic

activities for HER. The role of inter-layer potential or internal field is studied previously to show the systematic shift in the redox energy of $Ti^{4+/3+}$ redox couples in the layered perovskite $NaLnTiO_4$ (Ln = Y, La−Tb) for Li-ion intercalation. [38] In an earlier study, we also demonstrated the role of interlayer potential in stabilizing $Fe^{4+/2+}$ couple in orthorhombic $La_{1-x}K_xFeO_3$ perovskite resulting in superior pseudocapacitive charge storage. [39]

A series of poly-crystalline layered perovskite sodium yttrium titanate $Na_{1-x}K_xYTiO_4$ (x = 0, 0.1 & 0.2) and $NaY_{1-y}Gd_yTiO_4$ (y = 0.1, 0.2) has been synthesized by the sol-gel method and studied as an electrocatalyst for HER for the very first time. Electrochemical studies show that the HER activity of $NaYTiO_4$ is superior than TiO_2 which is due to interlayer potential exerted on distorted (elongated) TiO_6 octahedra present in between the alternate rocksalt of Na^+-O^{2-} and Y^{3+}-O^{2-} layers in the $NaYTiO_4$ lattice. Electrochemical studies reveal good HER performance of the $NaYTiO_4$ catalyst with an overpotential of 148 mV and a Tafel slope of 102 mV/dec with high stability. Furthermore due to the increase in strength of the interlayer dipolar electric field (interlayer potential) $NaY_{0.8}Gd_{0.2}TiO_4$ (overpotential: 106 mV, Tafel slope: 90 mV/dec) showed superior activity than $NaYTiO_4$.

5.2. Experimental Section

5.2.1. Material Synthesis

The $NaYTiO_4$ and series of doped compound $Na_{1-x}K_xYTiO_4$ (x = 0, 0.1 and 0.2) and $NaY_{1-y}Gd_yTiO_4$ (y = 0.1 and 0.2) were synthesized using a facile sol-gel method. Analytical reagents Na_2CO_3, K_2CO_3, yttrium nitrate hexahydrate (yttrium precursor), Gd_2O_3 (gadolinium precursor) and titanium isopropoxide $(C_3H_7O)_4Ti$ (titanium precursor) were used as starting materials. Citric acid (the molar ratio of metal ions to citric acid is 1:4) was used to form a gelatinous solution.

Typically, 3.05 mL titanium isopropoxide ($C_{12}H_{28}O_4Ti$ Sigma Aldrich 97%), and 1.918 g yttrium nitrate hexahydrate ($Y(NO_3)_3 \cdot 6H_2O$, Sigma Aldrich 99.8%) were sequentially dissolved into 25 mL dilute HNO_3 at 70 ℃ under stirring on a hot plate to form a homogenous solution A. 0.532 g sodium carbonate (Na_2CO_3 Merck 99.5%) was added in solution A, followed by adding 8.49 g citric acid monohydrate ($C_5H_8O_{10} \cdot H_2O$, Sigma Aldrich 99%) under constant stirring to get the final gelatinous solution. The final solution was placed into an oven at 80 ℃ for 4 h to evaporate the solvent and heated up to 120 ℃ for 12 h for polymerization. The dried gel was ground and kept in a furnace at 600 ℃ for 4 h, the obtained white sample was well grounded and divided into several parts and transferred to the furnace to heat at 750, 850 and 900 ℃, respectively for 3 h, with a heating rate of 3 ℃. The sample heated at 750 and 850 ℃, contains unreacted TiO_2 and pure-phase was obtained at 900 ℃ for 3 hours. The sintered sample was ground and further used for electrochemical testing.

5.3. Results and Discussion

5.3.1. XRD Studies and Rietveld Refinement

$Na_{1-x}K_xYTiO_4$ (x = 0, 0.1 and 0.2) and $NaY_{1-y}Gd_yTiO_4$ (y = 0.1, 0.2) were synthesized using the sol-gel method because the sol-gel method can produce smaller particle sizes compared to the conventional solid-state method. To optimize the synthesis condition, dry powder of $NaYTiO_4$, after gelation, was calcined at 750 ºC and 800 ºC for 3 hours and at 900 ºC for 3 and 6 hours. The powder XRD pattern of $NaYTiO_4$ prepared at different synthesis conditions is presented in **Figure 5.2**.

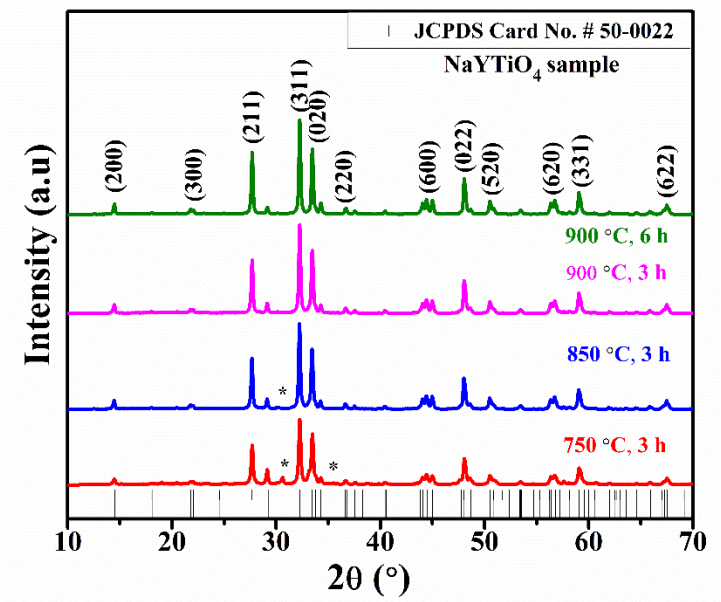

Figure 5.2 Powder XRD pattern of $NaYTiO_4$ with optimization of different sintering conditions.

Small impurities of unreacted phases were found in the XRD pattern of $NaYTiO_4$ calcined up to 800 ^oC. Single-phase crystalline $NaYTiO_4$ powder was obtained at 900 ^oC for 3 h of calcination. Powder XRD patterns of $Na_{1-x}K_xYTiO_4$ (x = 0, 0.1, 0.2) and $NaY_{1-y}Gd_yTiO_4$ (y= 0.1, 0.2) samples recorded in the range 2θ = 10-70^o , in **Figure 5.3a**, indicates the formation single phase crystalline material in orthorhombic phase, space group: *Pbcm* (57), peaks are well matched with JCPDS file (JCPDS No.: 50-0022). An enlarged image of the powder XRD plot showing peak shifting of (311) diffraction peak is plotted in **Figure 5.3b**. The powder XRD pattern of $NaYTiO_4$ was fitted through the Le Bail method to get the phase identification and structural parameters. Using the Le Bail parameters, the structure was refined using the GSAS + EXPGUI program. **Figure 5.3c** shows the Rietveld refined XRD profile of $NaYTiO_4$. All the diffraction peaks matched well with the orthorhombic phase, space group: *Pbcm* (57) (JCPDS No.: 50-0022), indicating the single-phase formation of the materials. Refined structural parameters of $NaYTiO_4$ obtained from Rietveld refinement are given in **Table 5.1**. The XRD of the anatase phase of synthesized TiO_2 is represented in **Figure 5.4**.

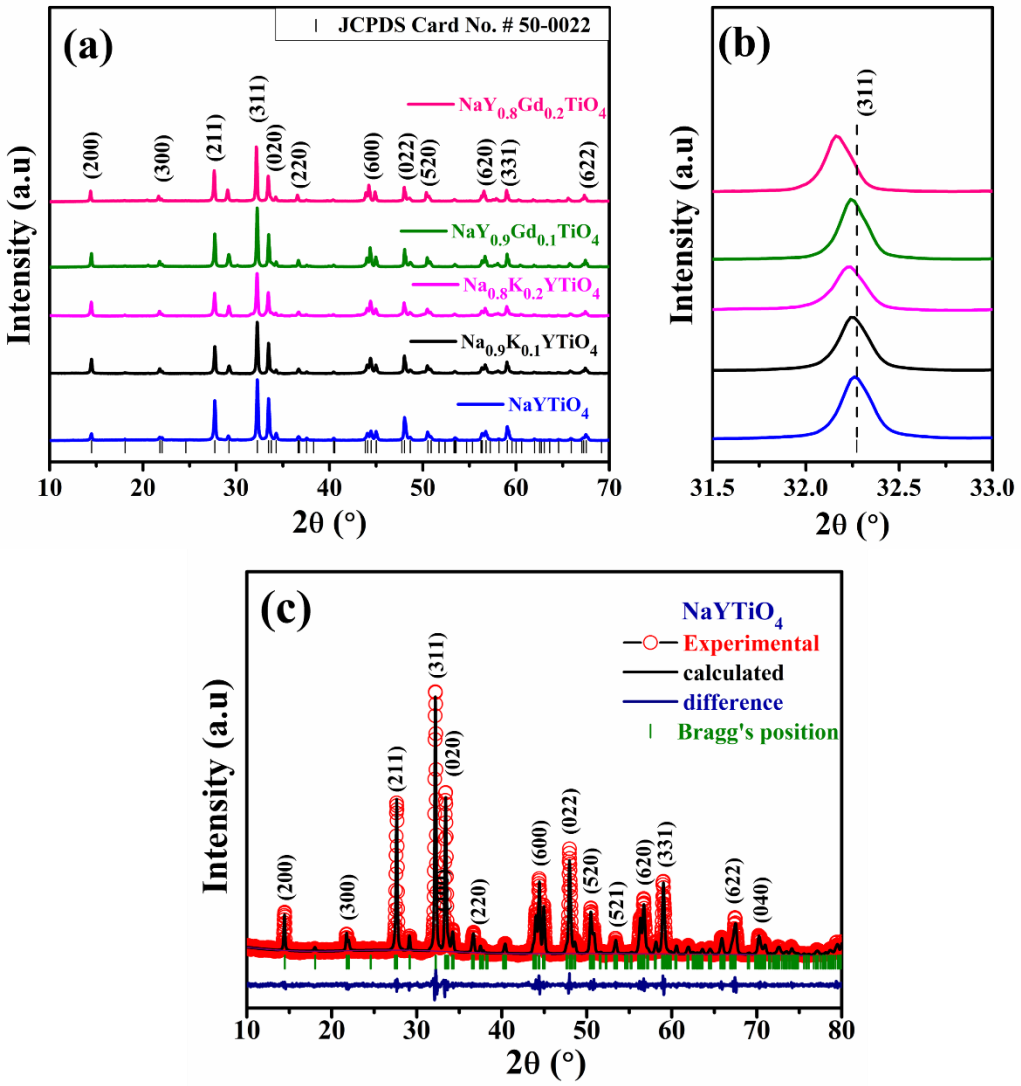

Figure 5.3. (a) XRD profile of all the samples $Na_{1-x}K_xYTiO_4$ (x= 0, 0.1, 0.2) and $NaY_{1-y}Gd_yTiO_4$ (y= 0.1, 0.2) , **(b)** Magnified image of the (311) peak & **(c)** Rietveld refined powder XRD pattern of $NaYTiO_4$

Table 5.1: Structural parameters of $NaYTiO_4$ based on Rietveld refinement.

Catalyst	a (Å)	b (Å)	c (Å)	$\alpha = \beta = \gamma$	χ^2	Rp	Rwp	GOF
$NaYTiO_4$	12.22	5.35	5.35	90°	1.75	0.06	0.08	1.32

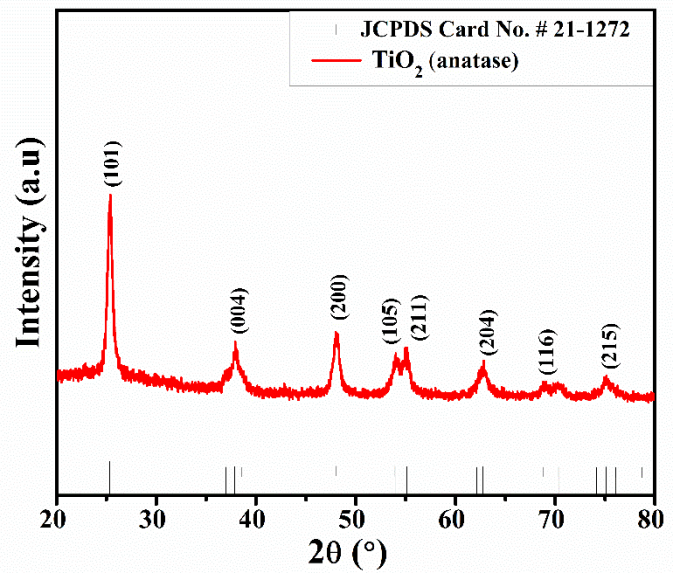

Figure 5.4. XRD of TiO_2 (anatase).

5.3.2. Raman and FTIR Analysis

FTIR spectrum (**Figure 5.5a**) of $NaYTiO_4$ shows a strong symmetrical stretching of the Ti–O bond at ~ 880 cm^{-1}. [40] The most striking feature in Raman spectra (**Figure 5.4b**) of $NaYTiO_4$ is a strong band at ~ 900 cm^{-1}, which is attributed to the symmetrical stretching mode of the short Ti–O bond and the band around 600 cm^{-1} was due to the asymmetric stretching mode of same Ti–O bond. Further, the bands below 400 cm^{-1} were observed due to the external modes located in the $(YO)_2$ layer. [40-41]

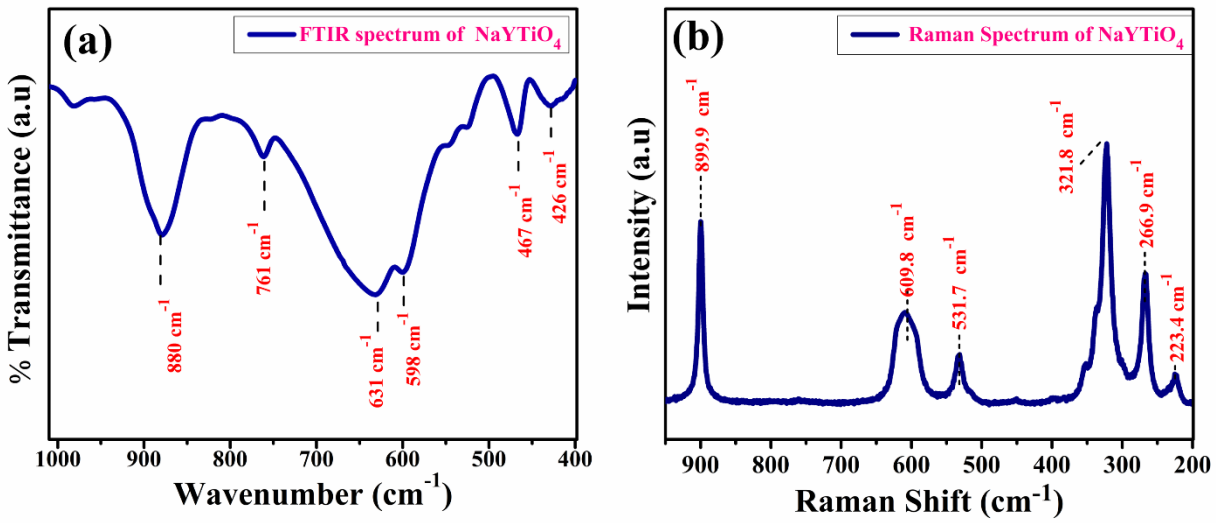

Figure 5.5. (a) FTIR spectrum of $NaYTiO_4$ & **(b)** Raman spectrum of $NaYTiO_4$.

5.3.3. XPS Studies

To study the electronic state of elements present in the $NaYTiO_4$ sample, X-ray photoelectron spectroscopy (XPS) was employed and the survey spectrum confirming the presence of all the elements is shown in **Figure 5.6**.

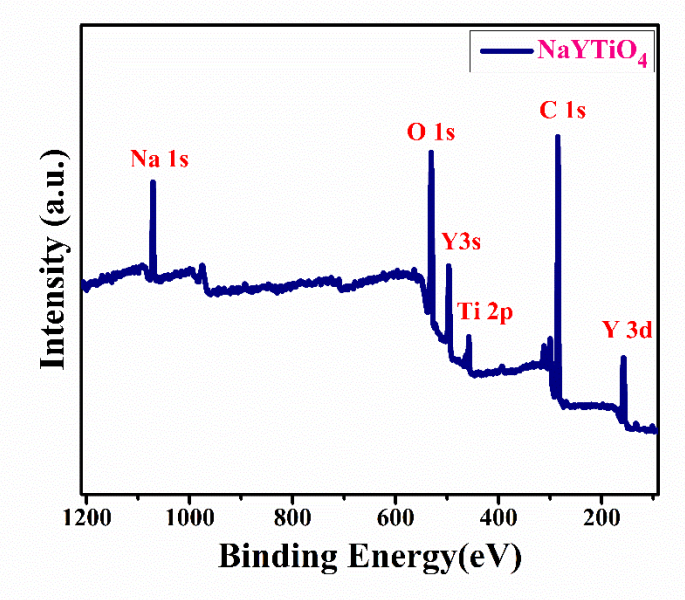

Figure 5.6. XPS full survey scan of $NaYTiO_4$ powder sample

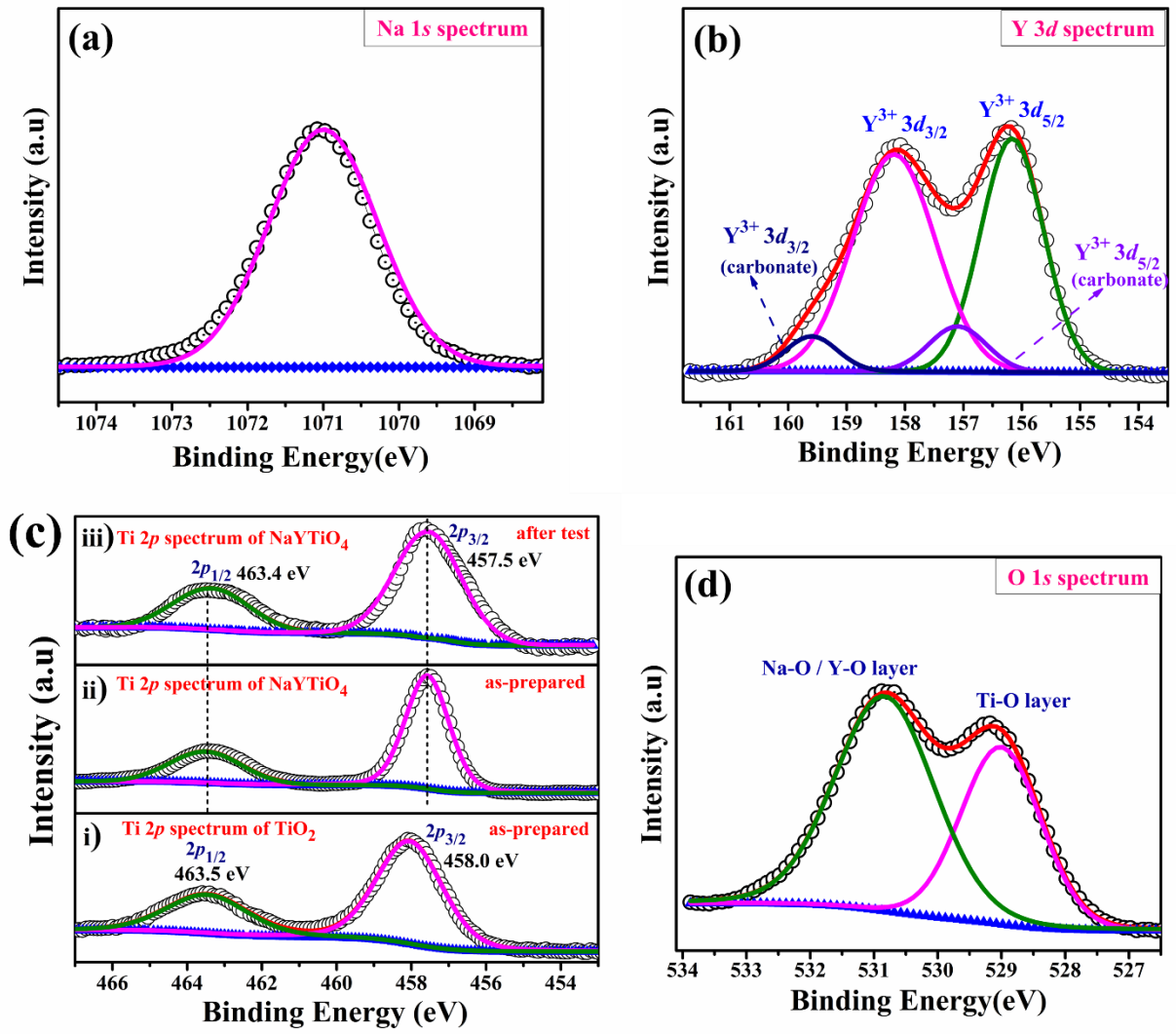

Figure 5.7. (a) Na (1*s*) core level spectrum, **(b)** Y (3*d*) core level spectrum, **(c)** comparative Ti (2*p*) core level spectrum of **(i)** as-prepared sample of TiO_2, **(ii)** as-prepared sample of $NaYTiO_4$, and **(iii)** $NaYTiO_4$ after testing (post HER) & **(d)** O (1*s*) core level spectrum peak at corresponding to lattice oxygen and adsorbed oxygen.

The Na (1*s*) spectra of $NaYTiO_4$ is given in **Figures 5.7a**. The binding energy value of Na (1*s*) is found to be at ~1070.9 eV. The Y 3*d* spectrum displays two sets of doublets (**Figure 5.7b**) which are fitted into two pairs of peaks, one pair corresponds to the Y^{3+} of yttrium oxide for which binding energy is located at 156.1 and 158.1 eV corresponding to the spin–orbit doublets $3d_{5/2}$ and $3d_{3/2}$ respectively, and the other pair corresponds to the Y^{3+} at ~159.1 eV ($3d_{3/2}$) and ~156.9 eV ($3d_{5/2}$)

due to surface yttrium carbonate formation. [42] **Figure 5.7c** represents The Ti (2*p*) spectrum in anatase TiO_2 and in $NaYTiO_4$ samples before and after HER testing. Ti $2p_{3/2}$ and $2p_{1/2}$ peaks appeared at 458 and 463.5 eV respectively for anatase TiO_2 and peaks appeared at 457.5 and 463.4 eV respectively for the as-prepared samples of $NaYTiO_4$ confirming the presence of Ti as Ti^{4+} in the sample. [42, 43] The little lower Ti ($2p_{3/2}$, $2p_{1/2}$) peaks for Ti^{4+} in $NaYTiO_4$ compared to TiO_2 is due to the strong ionic interaction O with Y and Na ion in the sample that reduces the iconicity of Ti–O bond that reduces the binding energy of Ti 2*p* states in the sample. The XPS spectrum of Ti($2p_{3/2}$, $2p_{1/2}$) after HER testing does not show any shift in the peak positions indicating that Ti remains in the same oxidation state of +4. The deconvoluted O (1*s*) spectrum of $NaYTiO_4$ (given in **Figures 5.7d**) consists of two peaks centered at ~529.1 and ~530.8 eV, confirming the presence of two types of oxygen in the lattice. The strong ionically bonded oxygen with Na and Y showed higher binding energy compared to oxygen bonded with Ti. Thus the combined XPS study of Ti ($2p_{3/2}$, $2p_{1/2}$) and O(1*s*) state shows the effect of interlayer potential on Ti–O octahedra. Due to the interlayer dipolar electric field (interlayer potential) on the TiO_6 octahedra present in between the $(NaO)_2^{2-}$ and $(YO)_2^{2+}$ rock salt layer (**Figure 5.1**), the Ti^{4+} (2*p*) core level position of $NaYTiO_4$ is found to be shifted to lower binding energy compared to TiO_6 octahedra in anatase TiO_2.

5.3.4. Microstructural Analysis

The morphology and particle size distribution of the $NaYTiO_4$ sample is determined from the scanning electron micrographs. The HR-SEM image of $NaYTiO_4$ is shown in **Figure 5.8a**, which depicts the uniform and slightly tetragonal, prismatic and bipyramidal-shaped particle distributed in the entire region of the micrograph. **Figure 5.8b** shows the energy dispersive X-ray analysis (EDX) image and the analysis confirms the nominal composition of elements Na, Ti, Y and O of $NaYTiO_4$. **Figure 5.8b (i-iv)** shows the elemental color mapping of Na, Ti, Y and O

atoms. Furthermore, since SEM-EDX cannot effectively give the element content, the relative concentration of Na, Ti and Y in the samples was also confirmed by the ICP mass spectrometry (ICP−MS) study. The relative concentration of the Na, Ti and Y obtained from ICP-MS studies are listed in **Table 5.2**.

Table 5.2: ICP-MS Result:

Element	Na (wt %)	Ti (wt %)	Y (wt %)
$NaYTiO_4$ Catalyst	10.26 ± 0.01	39.72 ± 0.01	21.39 ± 0.01

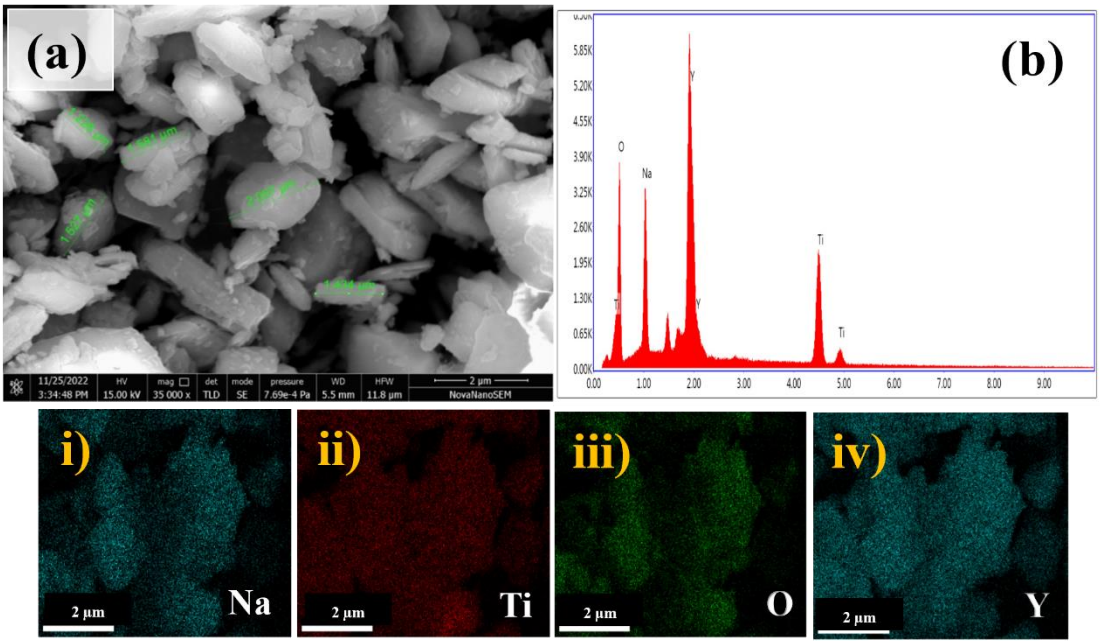

Figure 5.8 (a) HR-SEM image showing morphology of $NaYTiO_4$ powder sample, **(b)** EDX spectrum of $NaYTiO_4$, **(i-iv)** corresponding elemental colour mapping of individual elements (Na, Ti, O and Y, respectively)

HR-SEM images shown in **Figure 5.9** of $NaYTiO_4$ as-prepared (before) and after long-term cathodic cycling reveal not much change in particle size and shape/morphology of the material, confirming the morphological stability of material after testing.

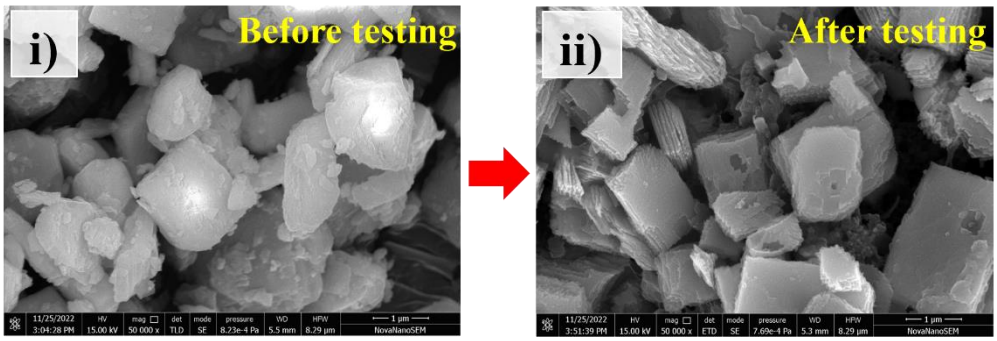

Figure 5.9 HR-SEM images of $NaYTiO_4$ (as-prepared) before and after HER-CA testing showing the morphology is retained after the electrochemical testing.

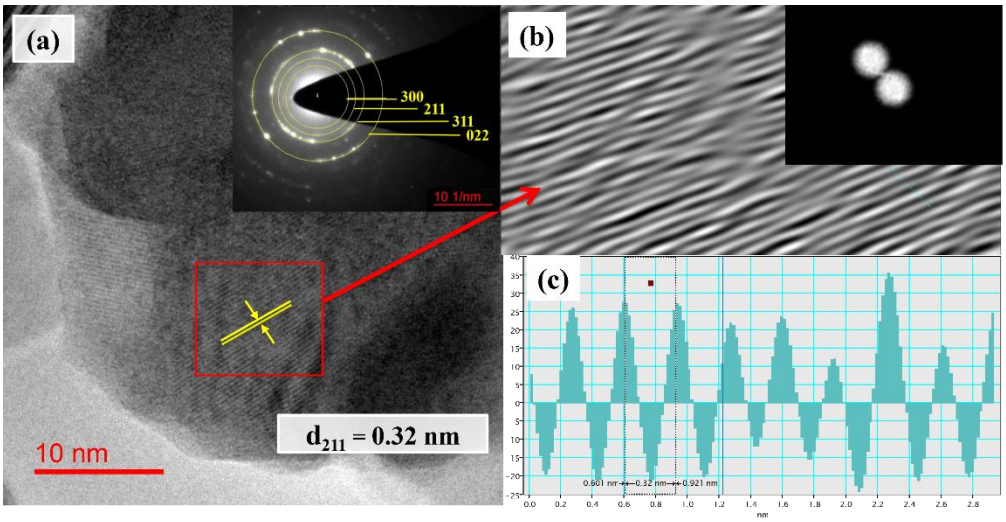

Figure 5.10 (a) HR-TEM image comprising the plane with lattice fringes; inset: SAED pattern, **(b)** FFT and inverse FFT of the selected region of (211) plane & **(c)** line profile of (211) plane with its *d*-spacing value.

The high-resolution-TEM images shown in **Figure 5.10a** represent lattice arrangements at the localized region of the powder sample. The calculated interplanar *d*-spacing was found to be 0.32 nm corresponding to the (211) plane (see the FFT and inverse FTT in **Figure 5.10b & c**).

5.3.5. Specific Surface Area Measurement

The BET surface area measurement plots of $NaYTiO_4$ are shown in **Figure 5.11a**. The nitrogen adsorption/desorption isotherm shows characteristics that correspond to the microporous

structure of the $NaYTiO_4$ sample. The calculated BET-specific surface area from the isotherms was found to be 4.37 m^2/g of powder sample. The pore size distribution curves shown in the inset indicate the presence of micropores with pore sizes ranging from 1 to 2 nm.

5.3.6. UV-Vis Analysis

A comparative UV-vis absorption spectrum, **Figure 5.11b**, of anatase TiO_2 and $NaYTiO_4$ powder samples show the band gap of 3.2 eV and 4.06 eV, respectively. UV-vis absorption spectra for all the samples are recorded in the range of 230–800 nm shown in **Figure 5.11c**. The band gap of the samples $Na_{1-x}K_xYTiO_4$ (x = 0.1, 0.2) and $NaY_{1-y}Gd_yTiO_4$ (y = 0.1, 0.2) was calculated from Tauc plot, in **Figure 5.11d**, and found to be 4.09, 4.18 eV and 3.96, 3.94 eV respectively.

5.3.7. Mott−Schottky Analysis

To determine the flat band potential (E_{fb}), the Mott−Schottky experiment were performed. The E_{fb} is the applied potential at which the Fermi level is placed at the same energy near the electrolyte redox potential. E_{fb} is the parameter that provides the electrochemical interface potential between the electrode and the electrolyte. [44-45] A frequency of 100 Hz was used in the range 0.05 to -0.4 V and 0 to -0.8 V for $NaYTiO_4$ and TiO_2 respectively, in the 0.5 M H_2SO_4 electrolyte as shown in **Figure 5.12a**. The positive slope of the Mott−Schottky plot indicates that both $NaYTiO_4$ and TiO_2 are n-type semiconductors. The E_{fb} of $NaYTiO_4$ and TiO_2 was obtained from intercept made on the *x*-axis from the plot of $1/C^2$ *vs* potential and found to be -0.186 and -0.447 V respectively. Mott−Schottky experiment for samples $Na_{0.8}K_{0.2}YTiO_4$ and $NaY_{0.8}Gd_{0.2}TiO_4$ recorded in the range of 0 to -0.4 V *vs* RHE at a frequency of 100 Hz (**Figure 5.12b**). E_{fb} for these two samples obtained from intercept made on the *x*-axis from the plot of $1/C^2$

vs potential and found to be -0.22 and -0.16 V respectively indicating that materials are *n*-type semiconductors.

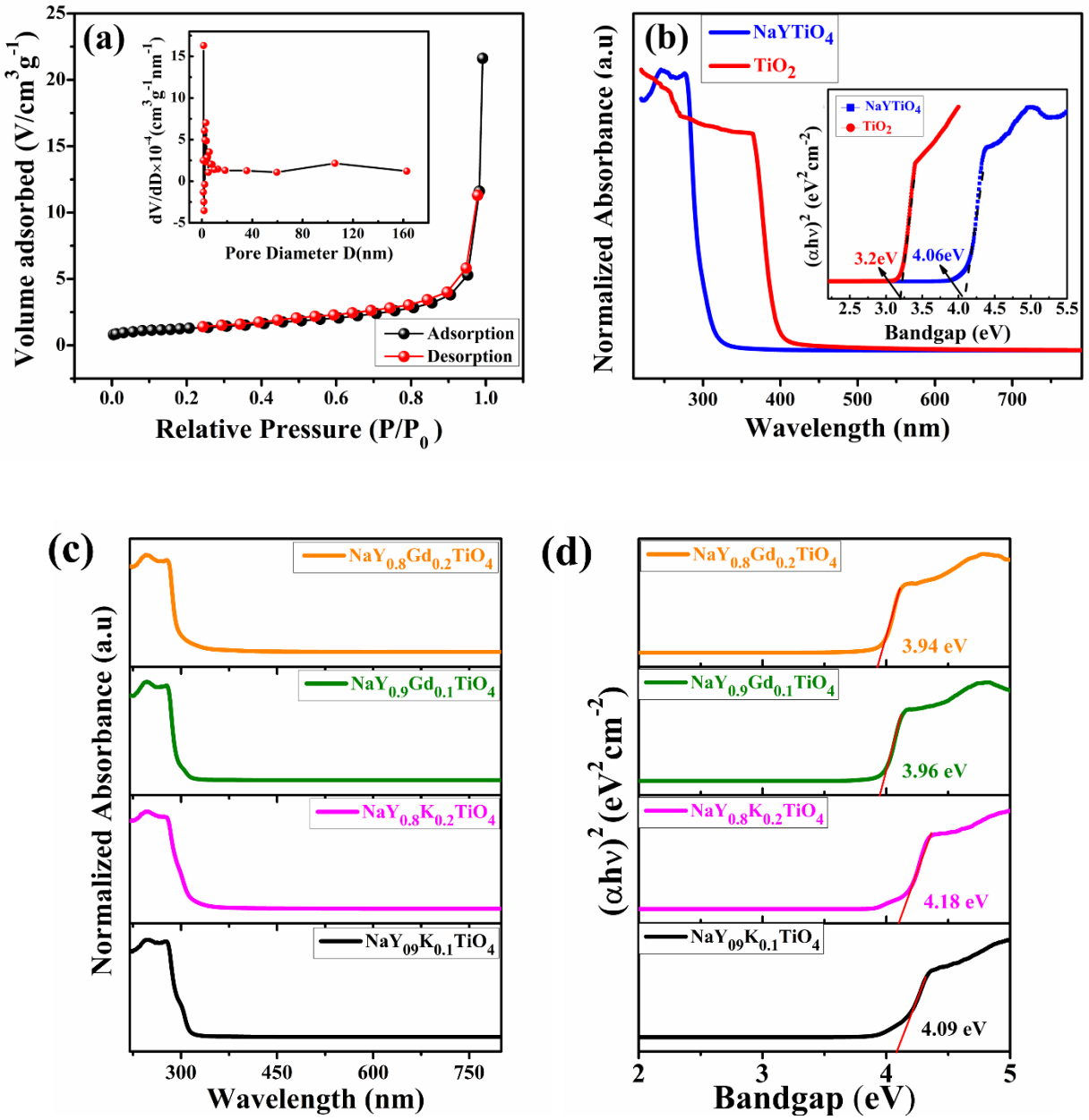

Figure 5.11 (a) N_2 adsorption/desorption isotherm curve of $NaYTiO_4$; inset shows the pore size diameter, **(b)** comparative UV-vis absorption spectrum and bandgap (inset) of $NaYTiO_4$ and TiO_2 powder sample, **(c)** UV-vis absorption spectra of $Na_{1-x}K_xYTiO_4$ (x= 0.1, 0.2) and $NaY_{1-y}Gd_yTiO_4$ (y= 0.1, 0.2) catalysts & **(d)** corresponding Tauc plot of samples $Na_{1-x}K_xYTiO_4$ (x= 0.1, 0.2) and $NaY_{1-y}Gd_yTiO_4$ (y= 0.1, 0.2).

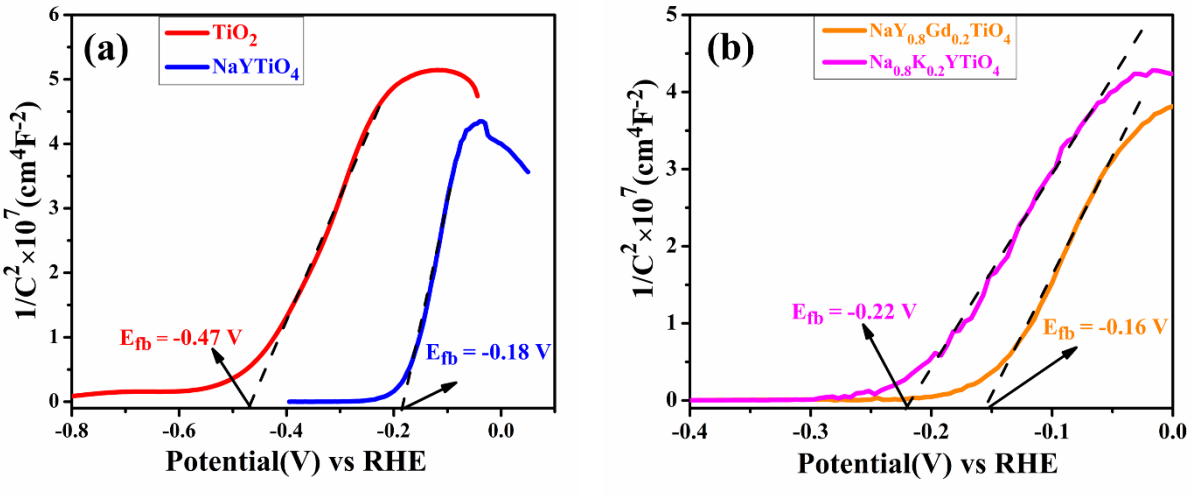

Figure 5.12 (a) the Mott-Schottky plot for $NaYTiO_4$ and TiO_2 & **(b)** Mott-Schottky plot for $Na_{0.8}K_{0.2}YTiO_4$ and $NaY_{0.8}Gd_{0.2}TiO_4$recorded at a frequency of 100 Hz.

The energy band diagram (**Figure 5.13**) was drawn with the help of the optical bandgap obtained from the UV-vis spectra **(Figure 5.11b,d)** and flat band potential calculated from the Mott-Schottky plot in **Figure 5.12a, b** respectively. The band diagram (**Figure 5.13)** shows schematic representations of the adjustment of the electronic structure, Ti(3*d*)-O(2*p*) hybridization or orbital overlap in Ruddlesden-Popper type $NaYTiO_4$ phase, due to built-up interlayer potential resulting in elongated/distorted TiO_6 octahedra; flat band potential (E_{fb}) or relative Fermi level (E_F) position decreases between Ti(3*d*)-O(2*p*) hybridization/band compared to Ti(3*d*)-O(2*p*) hybridization/band in anatase TiO_2. A decrease in the energy of relative Fermi level (E_F) or flat band potential (E_{fb}) favors the electron transfer activity near the conduction band that can enhance electrocatalytic activity, especially for ion reduction. [37-38], [45-49]

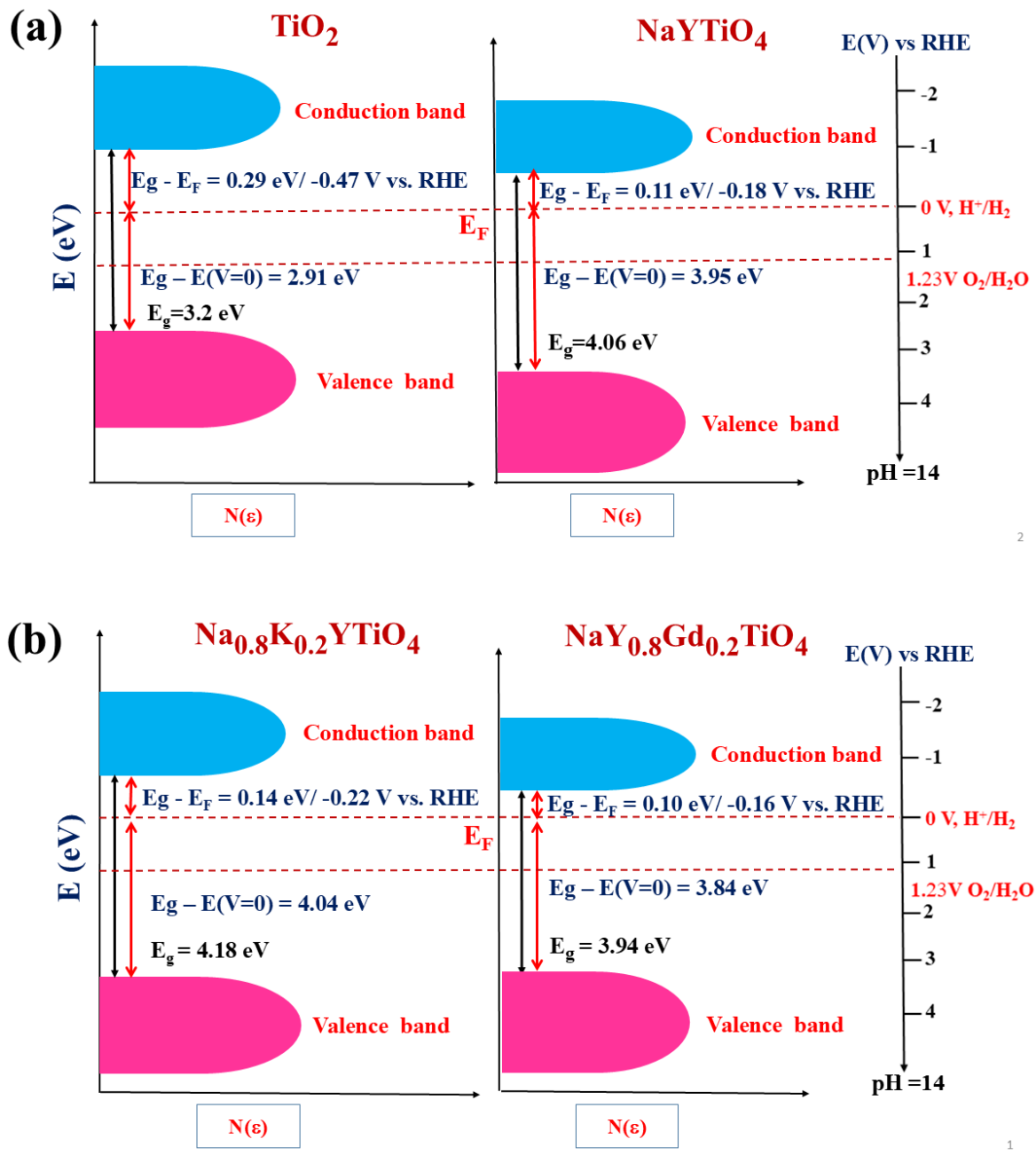

Figure 5.13 Schematic representation of the Ti(3*d*)/O(2*p*) orbital band for **(a)** $NaYTiO_4$ structure and anatase TiO_2 & **(b)** is for $Na_{0.8}K_{0.2}YTiO_4$ and $NaY_{0.8}Gd_{0.2}TiO_4$.

5.3.8. Electrochemical Studies

5.3.8.1 HER Performances of Synthesized Catalysts

The electrochemical performance of $Na_{1-x}K_xYTiO_4$ (x= 0, 0.1, 0.2) and $NaY_{1-y}Gd_yTiO_4$ (y= 0.1, 0.2), Pt/C and TiO_2 catalysts for HER was investigated in N_2-saturated 0.5 M H_2SO_4 electrolyte at a scan rate of 5 mVs^{-1} in a three-electrode setup.

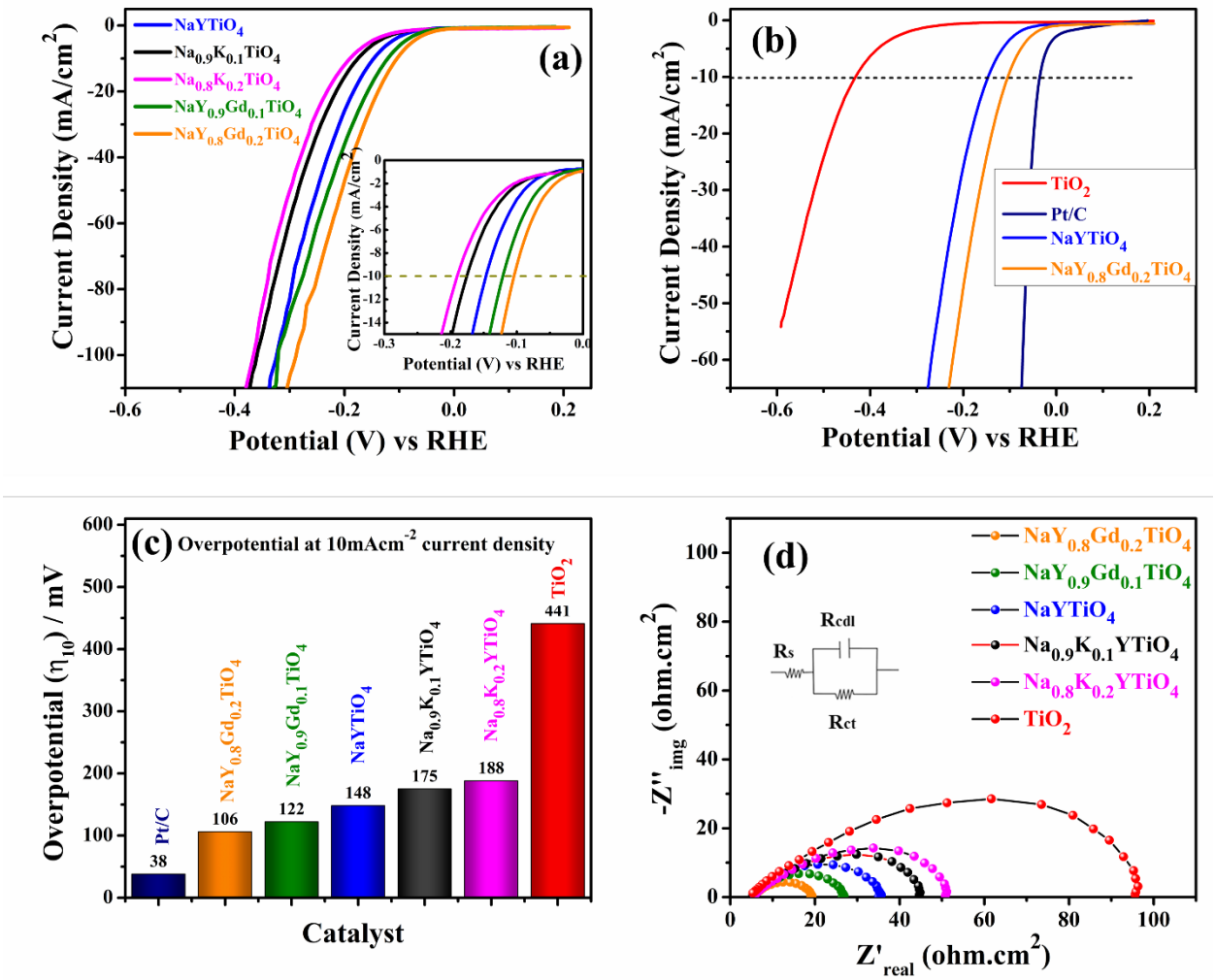

Figure 5.14. (a) HER LSV polarization profiles at a scan rate of 5 mv s^{-1}, **(b)** LSV polarizationprofiles of Pt/C, $NaYTiO_4$, $NaY_{0.8}Gd_{0.2}TiO_4$ and TiO_2 **(c)** overpotential at a current density of 10 mA cm^{-2}, **(d)** electrochemical impedance spectra recorded at respective overpotentials.

The linear sweep voltammogram (LSV) curve shown in **Figure 5.14a** represents HER performances of $Na_{1-x}K_xYTiO_4$ (x= 0, 0.1, 0.2), $NaY_{1-y}Gd_yTiO_4$ (y= 0.1, 0.2) and Pt/C, where Pt/C is a state-of-art HER electrocatalyst. LSV polarization profiles of Pt/C, $NaY_{0.8}Gd_{0.2}TiO_4$, $NaYTiO_4$ and TiO_2 are shown in **Figure 5.14b** for comparison. Overpotential for Pt/C, $NaY_{0.8}Gd_{0.2}TiO_4$, $NaY_{0.9}Gd_{0.1}TiO_4$, $NaYTiO_4$, $Na_{0.9}K_{0.1}YTiO_4$, $Na_{0.8}K_{0.2}YTiO_4$ and TiO_2 was found to be 38, 106, 122, 148, 175, 188 and 441 mV at 10 mA/cm^2 current density respectively shown in **Figure 5.14c**. Compared to TiO_2 (anatase), there is an almost 293 mV decrease in the overpotential of $NaYTiO_4$. The decrease in the overpotential is attributed to a shift/decrease in flat band potential (E_{fb}) or relative fermi level (E_F) position due to the presence of inter-layer potential in RP-phase $NaYTiO_4$. The effect of counter-cation in terms of introducing inter-layer potential is visible in decreasing the overpotential of the material for HER reactions. As the charge or ionicity of the cation vary, the strength of the dipolar electric field can be altered. K^+ is more ionic or electropositive than Na^+, thus with the substitution of K^+ on the Na^+ site, the Na^+/K^+-O^{2-} layer will become less electronegative, resulting decrease in the overall strength of the internal dipolar electric field or interlayer potential. Indeed, we found less catalytic HER activity for K-doped $NaYTiO_4$ ($Na_{1-x}K_xYTiO_4$) compared to $NaYTiO_4$. Similarly, Gd^{3+} is more ionic or electropositive than Y^{3+}, thus with the substitution of Gd^{3+} on the Y^{3+}site, the Y^{3+}/ Gd^{3+}–O^{2-} layer will become more electropositive, resulting increase in the overall internal dipolar electric field or interlayer potential. We found superior catalytic HER activity for Gd-doped $NaYTiO_4$ ($NaY_{1-x}Gd_xTiO_4$) compared to $NaYTiO_4$. Thus tuning the interlayer potential with a selection of suitable active cations can result in superior catalytic activity and electron transfer rates, it can be a very important area to explore for electrochemists and material scientists. Further electrochemical impedance spectroscopy (EIS) measurements were employed to evaluate the charge-transfer resistance of

catalysts. Electrochemical impedance studies for all the catalysts; $NaY_{1-y}Gd_yTiO_4$ (y= 0.1, 0.2), $Na_{1-x}K_xYTiO_4$ (x= 0, 0.1, 0.2), and TiO_2 were conducted in a frequency range of 0.1 Hz to 100 kHz with an AC amplitude of 10 mV at a potential of 125, 110, 150, 175, 190 and 445 mV respectively, shown in **Figure 5.14d**. An equivalent circuit fit of the EIS data is also provided in the inset of **Figure 5.14d**, which contains a solution resistance (R_s), a charge-transfer resistance (R_{ct}) and a double-layer capacitance (R_{Cdl}). The R_{ct} of $NaY_{1-y}Gd_yTiO_4$ (y= 0.1, 0.2), are 20.8and 13.5Ω respectively, and $Na_{1-x}K_xYTiO_4$ (x= 0, 0.1, 0.2) are 29.8, 39. and 45 Ω respectively. The R_{ct} of $NaYTiO_4$ (29.8 Ω) and $NaY_{0.8}Gd_{0.2}TiO_4$ (13.5Ω) is much smaller than TiO_2 (90.4 Ω). The lower R_{ct} value for $NaYTiO_4$ indicates its faster charge transfer rate and superior HER kinetics. The cathodic reaction in the acidic medium for the water electrolysis is the reduction of hydronium ions (H_3O^+) to gaseous dihydrogen (H_2). From a thermodynamic point of view, this multi-step electrode reaction should occur at the potential of the reference hydrogen electrode (RHE). The evolution of molecular H_2 is followed by steps given below, [47]

(Volmer step) $H_3O^+ + e^- + * = H^* + H_2O$ (5.1)

(Heyrovsky step) $H^* + H_3O^+ + e^- = H_2 + H_2O$ (5.2)

(Tafel step) $2H^* = H_2$ (5.3)

where * denotes an active site on the catalyst surface, and H* is a hydrogen atom adsorbed on an active site. The Tafel slope value is an important parameter to determine the kinetics of hydrogen evolution reaction. To investigate the electrocatalytic reaction kinetics during the HER process, the Tafel plot was derived from the LSV curve. Tafel plots are fitted using the following Tafel equation.

$$\eta = b\ log|\ j\ | + a \quad (5.4)$$

where η is overpotential, j is current density (mA.cm^{-2}), b is Tafel slope and a is exchange current density. The Tafel plot of $Na_{1-x}K_xYTiO_4$ (x= 0, 0.1, 0.2) and $NaY_{1-y}Gd_yTiO_4$ (y= 0.1, 0.2) catalysts are shown in **Figure 5.15a** was accordingly calculated to examine the HER kinetics.

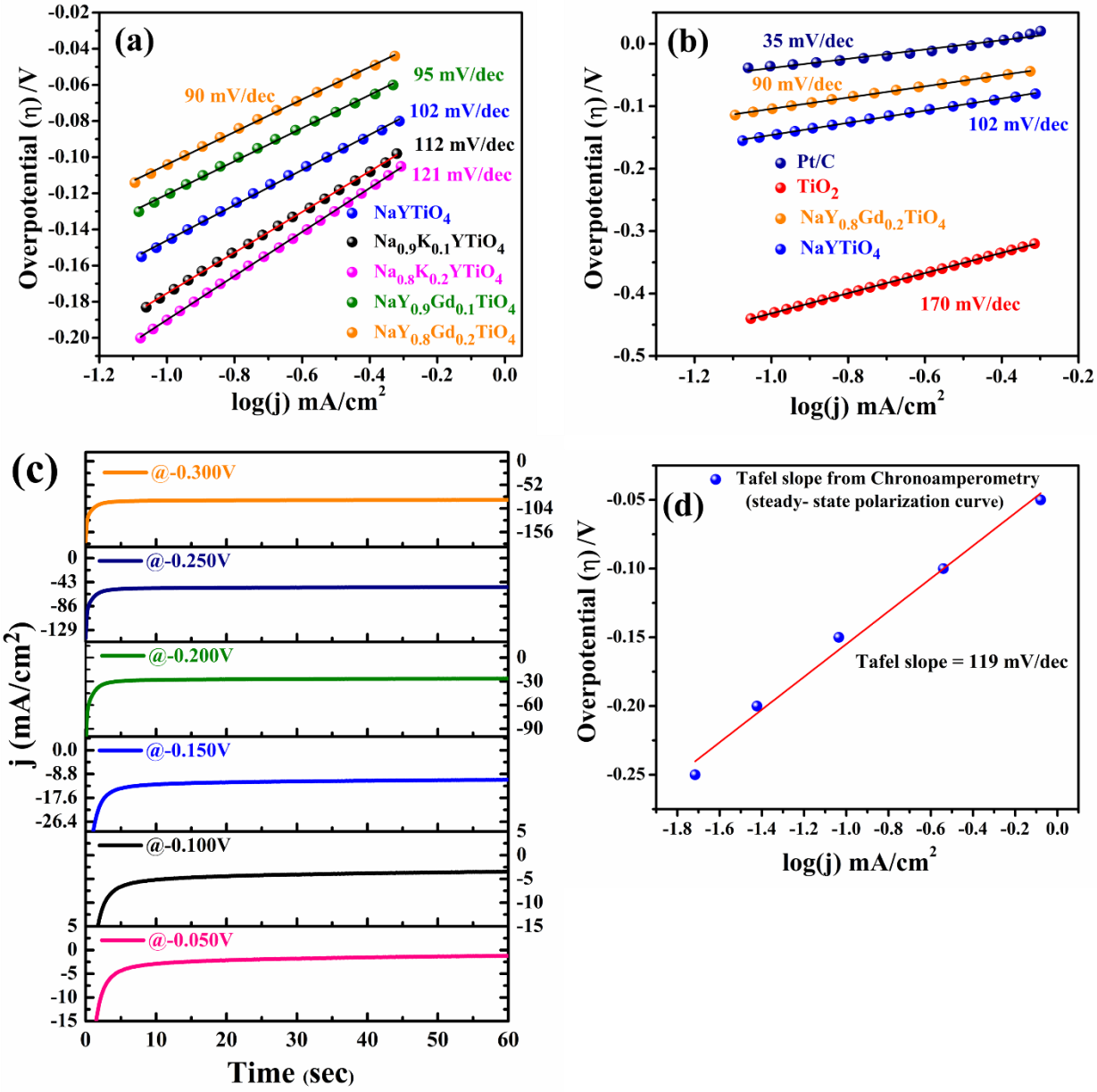

Figure 5.15. (a) Tafel plots of $Na_{1-x}K_xYTiO_4$ (x= 0, 0.1, 0.2) and $NaY_{1-y}Gd_yTiO_4$ (y= 0.1, 0.2) **(b)** comparative Tafel plots for Pt/C, $NaYTiO_4$ $NaY_{0.8}Gd_{0.2}TiO_4$ & TiO_2, **(c)** steady-state polarisation curve of $NaYTiO_4$ recorded by holding the given potential for 60 sec & **(d)** Tafel slope of $NaYTiO_4$ calculated from chronoamperometry.

Tafel slope of $Na_{1-x}K_xYTiO_4$ (x = 0.1 and 0.2), $NaYTiO_4$ and $NaY_{1-y}Gd_yTiO_4$ (y = 0.1 and 0.2) samples was found to be 112, 121, 102, 95 and 90 mV dec^{-1} respectively. **Figure 5.15b** shows the Tafel slope of (102 mV dec^{-1}) of $NaYTiO_4$ and $NaY_{0-8}Gd_{0.2}TiO_4$ (90 mV dec^{-1}) is much lower than the Tafel slope (170 mV dec^{-1}) of TiO_2, and is close to the Tafel slope (35 mV dec^{-1}) of Pt/C, a model electrocatalyst, suggesting the excellent hydrogen evolution activity of $NaYTiO_4$ and Gd doped $NaYTiO_4$. Tafel slope value 102 mV dec^{-1} for $NaYTiO_4$ suggests the Volmer-Heyrovsky reaction pathway is the rate-determining step for the HER. [48] As the Tafel slope calculated from the potentiodynamic polarisation curve is not precise/true slope value so we calculated the Tafel slope from the potentiostatic curve (chronoamperometry, CA) i.e. true steady state polarisation curve. The potentiostatic curve for $NaYTiO_4$ was recorded by holding the potential for 60 sec each and increasing the potential by 50 mV each time as shown in **Figure 5.15c**. From the steady-state CA responses plotted in the **Figure 5.15d**, the fitted value gave the tafel slope value of 119 mV dec^{-1} which is comparable to 102 mV dec^{-1} obtained from LSV. A comparative table for different HER active electrocatalysts in terms of overpotential and Tafel slope is summarised in **Table 5.3**. [49-55] HER activity of $NaYTiO_4$ and $NaY_{1-y}Gd_yTiO_4$ is not only superior to anatase TiO_2, but the activity of the electrocatalyst is superior or at least equivalent to most of the oxide electrocatalysts studied for HER. Electrochemical surface area (ECSA) is evaluated to investigate the intrinsic properties of the $NaYTiO_4$ electrocatalyst. With $NaYTiO_4$ as the working electrode, cyclic voltammetry (CV) in non-faradic potential range from 0.709 to 0.809 V with different scan rates ranging from 40 to 140 mV/s was studied and shown in **Figure 5.16a**. Change in current density (ΔJ) for anodic and cathodic scans in CV depends on the charge-storing ability of the working electrode and it increases linearly on increasing the scan rate. The double-layer capacitance which is half of the slope of ΔJ *vs* η plot is found to be 11.5 mF/cm^{-2} (**Figure 5.16b**) for $NaYTiO_4$.

Table 5.3: HER activity comparison table for some representative catalysts, including Ti-based catalysts and Perovskite-family-based metal oxides:

Electrocatalyst	Substrate	Electrolyte	η_{10} (mV)	Tafel slope ($mVdec^{-1}$)	Reference
Ti-based catalysts					
$TiO_{1.23}$	_	0.5 M H_2SO_4	198	88	37
α-Ti_2O_3	_	0.5 M H_2SO_4	495	241	38
Y-Ti_2O_3	_	0.5 M H_2SO_4	271	199	38
Ti_3CNT_x	Glassy carbon	0.5 M H_2SO_4	53	86	56
Perovskite-family based Metal oxides					
Sr_2RuO_4	Glassy carbon	1 M KOH	61	51	57
SNCF-NR	Glassy carbon	1 M KOH	232	103	58
Pr0.5BSCF	Glassy carbon	1 M KOH	237	45	59
$SrTi_{0.7}Ru_{0.3}O_{3-\delta}$ (STRO)	Glassy carbon	1 M KOH	46	40	60
$NaYTiO_4$	**Glassy carbon**	**0.5 M H_2SO_4**	**148**	**102**	**This Work**
$NaY_{0.8}Gd_{0.2}TiO_4$	**Glassy carbon**	**0.5 M H_2SO_4**	**106**	**90**	**This Work**
$Na_{0.8}K_{0.2}YTiO_4$	**Glassy carbon**	**0.5 M H_2SO_4**	**188**	**121**	**This Work**

5.3.8.2 Long-term Stability Test

The stability of electrocatalyst is an important parameter for large-scale water electrolysis applications. The potentiostatic stability of $NaYTiO_4$ was examined by performing a chronoamperometric (CA) test at -0.15 V *vs* RHE (**Figure 5.16c**) for 24 hours.

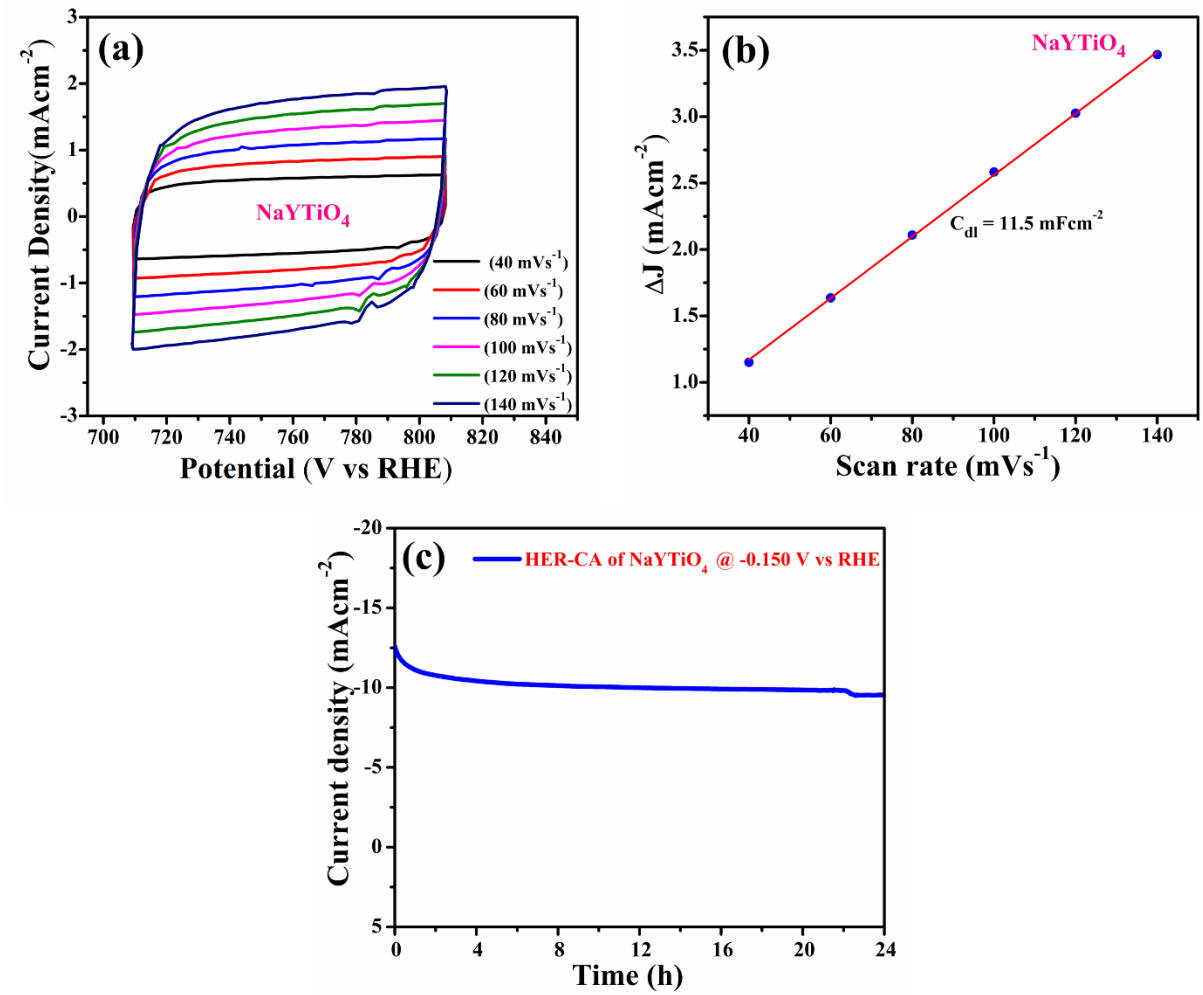

Figure 5.16. (a) CV measurements in a non-faradic current region (0.709-0.809 V *vs*. RHE) at different scan rates, **(b)** plot of scan rate *vs*. capacitive current density differences (ΔJ) for $NaYTiO_4$ and **(c)** chronoamperogram of $NaYTiO_4$ at an applied potential of -0.15 V *vs*. RHE.

Only a slight change in the current at the given potential was observed indicating excellent stability of electrocatalyst.

5.4. Conclusion

Tuning the relative position of the redox energies with Fermi levels in different oxides is important for designing novel electrocatalysts and electrodes for electrochemical conversion devices. The incorporation of interlayer potential to tune the relative redox energies of the Ti(IV)/Ti(III) redox couples in K and Gd doped $NaYTiO_4$ i.e. $Na_{1-x}K_xYTiO_4$ ($x \leq 0.2$) and $NaY_{1-y}Gd_yTiO_4$ ($x \leq 0.2$)

was envisaged here to develop a superior HER electrocatalyst. Poly-crystalline sodium yttrium titanate ($NaYTiO_4$), $Na_{1-x}K_xYTiO_4$ ($x \leq 0.2$), and $NaY_{1-y}Gd_yTiO_4$ ($x \leq 0.2$) were synthesized by the sol-gel method and presented as an efficient electrocatalyst for hydrogen evolution reaction for the very first time. Electrochemical studies reveal good HER activity of the electrocatalyst; HER activity $NaYTiO_4$ is not only superior to TiO_2 but also superior or at least equivalent to most of the oxide electrocatalyst studied for HER. Electrochemical studies reveal good HER performance of $NaYTiO_4$ with an overpotential of 148 mV and Tafel slope 102 mV/dec with high stability during 24 hours of continuous chronoamperometry test at -0.15 V *vs*. RHE. Superior catalytic HER activity was obtained for high electropositive Gd-doped $NaYTiO_4$ ($NaY_{1-x}Gd_xTiO_4$) compared to $NaYTiO_4$. Thus tuning the interlayer potential with a selection of suitable active cations can result in superior specific catalytic activity and electron transfer rates and can be a very important area to explore for electrochemists and material scientists.

5.5. References

1. Bossel, U.; Eliasson, B. Energy and the Hydrogen Economy. *Eur. Fuel Cell Forum, Lucerne* **2002**, 1−36.
2. Dresselhaus, M. S.; Thomas, I. L. Alternative Energy Technologies, *Nature* **2001**, *414*, 332– 337.
3. Turner, J. A. Sustainable Hydrogen Production. *Science* **2004**, *305*, 972– 974.
4. Chu, S.; Majumdar, A. Opportunities and Challenges for a Sustainable Energy Future. *Nature* **2012,** *488*, 294– 303.
5. Yilanci, A.; Dincer, I.; Ozturk, H. K. A review on solar-hydrogen/fuel cell hybrid energy systems for stationary applications. *Prog. Energy Combust. Sci.* **2009**, *35*, 231– 244.
6. Turner, J.; Sverdrup, G.; Mann, M. K.; Maness, P. C.; Kroposki, B.; Ghirardi, M.; Evans, R. J.; Blake, D. Renewable hydrogen production. *Int. J. Energy Res.* **2008**, *32*, 379– 407.
7. Ye, G.; Gong, Y.; Lin, J.; Li, B.; He, Y.; Pantelides, S. T.; Zhou, W.; Vajtai, R.; Ajayan, P. M. Defects Engineered Monolayer MoS_2 for Improved Hydrogen Evolution Reaction. *Nano Lett.* **2016**, *16*, 1097– 1103.
8. Lee, S. C.; Benck, J. D.; Tsai, C.; Park, J.; Koh, A. L.; Abild-Pedersen, F.; Jaramillo, T. F.; Sinclair, R. Chemical and Phase Evolution of Amorphous Molybdenum Sulfide Catalysts for Electrochemical Hydrogen Production. *ACS Nano.* **2016**, *10*, 624– 632.
9. Lu, Q.; Yu, Y.; Ma, Q.; Chen, B.; Zhang, H. 2D Transition-Metal-Dichalcogenide-Nanosheet-Based Composites for Photocatalytic and Electrocatalytic Hydrogen Evolution Reactions. *Adv. Mater.* **2016**, *28*, 1917– 1933.
10. Lewis, N. S.; Nocera, D. G. Powering the planet: Chemical challenges in solar energy utilization. *Proc. Natl. Acad. Sci. U.S.A.* **2007**, *104*, 20142.
11. McKone, J. R.; Marinescu, S. C.; Brunschwig, B. S.; Winkler, J. R.; Gray, H. B. Earth-abundant hydrogen evolution electrocatalysts. *Chem. Sci.* **2014**, *5*, 865– 878.
12. Safizadeh, F.; Ghali, E.; Houlachi, G. Electrocatalysis developments for hydrogen evolution reaction in alkaline solutions – A Review. *Int. J. Hydrog. Energy.* **2015**, *40*, 256– 274.
13. Zou, X.; Zhang, Y. Noble metal-free hydrogen evolution catalysts for water splitting. *Chem. Soc. Rev.* **2015**, *44*, 5148– 5180.

14. Zheng, Y.; Jiao, Y.; Jaroniec, M.; Qiao, S. Z. Advancing the Electrochemistry of the Hydrogen-Evolution Reaction through Combining Experiment and Theory. *Angew. Chem. Int. Ed.* **2015**, *54*, 52– 65.
15. Morales-Guio, C. G.; Stern L. A.; Hu X. Nanostructured hydrotreating catalysts for electrochemical hydrogen evolution. *Chem. Soc. Rev.* **2014**, *43*, 6555-6569.
16. Bockris, J. M. The origin of ideas on a Hydrogen Economy and its solution to the decay of the environment. *Int. J. Hydrog. Energy.* **2002**, *27*, 731-740.
17. Guan, D.; Zhou, J.; Huang, Y. C.; Dong, C. L.; Wang, J. Q.; Zhou, W. and Shao Z. Screening highly active perovskites for hydrogen- evolving reaction via unifying ionic electronegativity descriptor. *Nat. Commun.* **2019**, *10*, 3755.
18. Levie, R. D. Short Communication The electrolysis of water. *J. Electroanal. Chem.* **1999**, *476*, 92–93.
19. Li, C.; Baek, J. B. Recent Advances in Noble Metal (Pt, Ru, and Ir)-Based Electrocatalysts for Efficient Hydrogen Evolution Reaction. *ACS Omega* **2020**, *5*, 31–40.
20. Liu, X.; Jiao, Y.; Zheng, Y.; Daveya, K.; Qiao, S. Z. A computational study on Pt and Ru dimers supported on graphene for the hydrogen evolution reaction: new insight into the alkaline mechanism, *J. Mater. Chem. A*. **2019**, *7*, 3648-3654.
21. Deng, J.; Ren, P.; Deng, D.; Yu, L.; Yang, F.; Bao, X. Highly active and durable non-precious-metal catalysts encapsulated in carbon nanotubes for hydrogen evolution reaction. *Energy Environ. Sci.* **2014**, *7*, 1919−1923.
22. Wu, H. B.; Xia, B. Y.; Yu, L.; Yu, X.-Y.; Lou, X. W. Porous molybdenum carbide nano-octahedrons synthesized via confined carburization in metal-organic frameworks for efficient hydrogen production. *Nat. Commun.* **2015**, *6*, 6512.
23. Tang, C.; Zhang, R.; Lu, W.; He, L.; Jiang, X.; Asiri, A. M.; Sun, X. Fe-Doped CoP Nanoarray: A Monolithic Multifunctional Catalyst for Highly Efficient Hydrogen Generation. *Adv. Mater.* **2017**, *29*, 1602441.
24. Yan, H.; Tian, C.; Wang, L.; Wu, A.; Meng, M.; Zhao, L.; Fu, H. Phosphorus-Modified Tungsten Nitride/Reduced Graphene Oxide as a High-Performance, Non-Noble-Metal Electrocatalyst for the Hydrogen Evolution Reaction. *Angew. Chem., Int. Ed.* **2015**, *54*, 6325−6329.

25. McAllister, J.; Bandeira, N. A. G.; McGlynn, J. C.; Ganin, A. Y.; Song, Y. F.; Bo, C.; Miras, H. N. Tuning and mechanistic insights of metal chalcogenide molecular catalysts for the hydrogen-evolution reaction. *Nat. Commun.* **2019**, *10*, 370.
26. Zheng, Y.; Jiao, Y.; Zhu, Y.; Li, L. H.; Han, Y.; Chen, Y.; Du, A.; Jaroniec, M.; Qiao, S. Z. Hydrogen evolution by a metal-free electrocatalyst. *Nat. Commun.* **2014**, *5*, 3783.
27. Fan, X.; Peng, Z.; Wang, J.; Ye, R.; Zhou, H.; Guo, X. Carbon- Based Composite as an Efficient and Stable Metal-Free Electrocatalyst. *Adv. Funct. Mater.* **2016**, *26*, 3621−3629.
28. Xi, M.; Lei, T.; Lv, N.; Li, N. Synthesis and electrocatalytic hydrogen evolution performance of Ni−Mo−Cu alloy coating electrode. *Int. J. Hydrog. Energy.* **2014**, *39*, 4794−4802.
29. Subbaraman, R.; Tripkovic, D.; Chang, K. C.; Strmcnik, D.; Paulikas, A. P.; Hirunsit, P.; Chan, M.; Greeley, J.; Stamenkovic, V.; Markovic, N. M. Trends in activity for the water electrolyzer reactions on 3d M(Ni, Co, Fe, Mn) hydr(oxy)oxide catalysts. *Nat. Mater*. **2012**, *11*, 550.
30. Xu, X.; Shao, Z.; and Jiang, S.P. High-Entropy Materials for Water Electrolysis. *Energy Technol.* **2022**, *10*, 2200573.
31. Abdelghafar, F.; Xu, X.; and Shao, Z. Designing single-atom catalysts toward improved alkaline hydrogen evolution reaction. *Materials Reports: Energy.* **2022**, 100144.
32. Chen, D.; Wang, J.; Zhang, Z.; Shao, Z.; and Ciucci, F. Boosting oxygen reduction/evolution reaction activities with layered perovskite catalysts. *ChemComm*. **2016**, *52*, 10739-10742.
33. Xu, X.; Pan, Y.; Zhong, Y.; Ran, R.; and Shao, Z. Ruddlesden–Popper perovskites in electrocatalysis. *Mater. Horiz.* **2020**, *7*, 2519-2565.
34. Yang, L.; Jiao, Y.; Xu, X.; Pan, Y.; Su, C.; Duan, X.; Sun, H.; Liu, S.; Wang, S.; and Shao, Z. Superstructures with Atomic-Level Arranged Perovskite and Oxide Layers for Advanced Oxidation with an Enhanced Non-Free Radical Pathway. *ACS Sustain Chem Eng*. **2022**, *10*, 1899-1909.
35. Goodenough, J. B.; Mapping of Redox Energies, *Molecular Crystals and Liquid Crystals Science and Technology. Section A. Molecular Crystals and Liquid Crystals*. **1998**, 311, 1-14.

36. Goodenough, J. B. Electronic and ionic transport properties and other physical aspects of perovskites. *Rep. Prog. Phys.* **2004**, *67*, 1915.
37. Zhu, Y.; Tahini, H. A.; Hu, Z.; Dai, J.; Chen, Y.; Sun, H.; Zhou, W.; Liu, M.; Smith, S. C.; Wang, H.; Shao, Z. Unusual synergistic effect in layered Ruddlesden−Popper oxide enables ultrafast hydrogen evolution. *Nat. Commun.* **2019**, *10*, 149.
38. Song, S. H.; Ahn, K.; Kanatzidis, M. G.; Alonso, J. A.; Cheng, J. G. and Goodenough, J. B. Effect of an Internal Electric Field on the Redox Energies of $ALnTiO_4$, (A = Na or Li, Ln = Y or Rare-Earth). *Chem. Mater.* **2013**, *25*, 3852−3857.
39. Mondal, R.; Mishra, N. K.; Maiyalagan, T.; Gupta, A. and Singh, P. $La_{1-x}K_xFeO_{3-\delta}$: An Anion Intercalative Pseudocapacitive Electrode for Supercapacitor Application. *ACS Omega* **2021**, *6*, 30488−30498.
40. Blasse, G.; and Van Den Heuvel, G. P. M. Vibrational spectra and structural considerations of compounds NaLnTiO4. *J. Solid State Chem.* **1974**, *10*, 206-210.
41. Byeon, S.H.; Lee, S.O.; and Kim, H. Structure and Raman spectra of layered titanium oxides. *J. Solid State Chem.* **1997**, *130*, 110-116.
42. Zhang, Y.; Huang, J.; Saito, N.; Yang, X.; Zhang, Z.; Yang, L.; and Hirano, S.I. Layered Perovskite Lithium Yttrium Titanate as a Low-Potential and Ultrahigh-Rate Anode for Lithium-Ion Batteries. *Adv. Energy Mater*. **2022**, *12*, 2200922.
43. Bakr, Z. H.; Wali, Q; Ismail, J; Elumalai, N. K; Uddin, A; Jose, R. Synergistic combination of electronic and electrical properties of SnO_2 and TiO_2 in a single SnO_2-TiO_2 composite nanofiber for dye-sensitized solar cells. *Electrochimica Acta* **2018,** *263*, 524-532.
44. Manzoli, A.; Eguiluz, K. I. B.; Salazar-Banda, G. R.; Machado, S. A. S. Electrodeposition and characterization of undoped and nitrogen-doped ZnSe films. *Mater. Chem. Phys.* **2010**, *121*, 58-62.
45. Mondal, R.; Ratnawat, H.; Mukherjee, S.; Gupta, A.; and Singh, P. Investigation of the Role of Sr and Development of Superior Sr-Doped Hexagonal $BaCoO_{3-\delta}$ Perovskite Bifunctional OER/ORR Catalysts in Alkaline Media. *Energy & Fuels*. **2022,** *36*, 3219-3228.
46. Wang, L.; Lee C. Y. and Schmuki, P. Solar water splitting: preserving the beneficial small feature size in porous α-Fe_2O_3 photoelectrodes during annealing. *J. Mater. Chem. A* **2013**, *1*, 212-215.

47. Dubouis N.; Grimaud, A. The hydrogen evolution reaction: from material to interfacial descriptors. *Chem. Sci.* **2019**, *10*, 9165.
48. Lu,Q.; Hutchings,G.; Yu, W.; Zhou,Y.; Forest, R.; Tao,R.; Rosen, J.; Yonemoto, Bryan T.; Cao, Z.; Zheng, H.; . Xiao, John Q.; Jiao, Feng.; & Chen, Jingguang G.; Highly porous non-precious bimetallic electrocatalysts for efficient hydrogen evolution. *Nat. Commun.* **2015**, *6*, 6567.
49. Swaminathan, J.; Subbiah R.; Singaram, V. Defect-Rich Metallic Titania ($TiO_{1.23}$)-An Efficient Hydrogen Evolution Catalyst for Electrochemical Water Splitting. *ACS Catal.* **2016**, *6*, 2222–2229.
50. Li, Y.; Yu, Z. G.; Wang, L.; Weng, Y.; Tang, C. S.; Yin, X.; Han, K.; Wu, H.; Yu, X.; Wong, L. M.; Wan, D.; Wang, X. R.; Chai, J.; Zhang, Y. W.; Wang, S.; Wang, J.; Wee, A. T. S.; Breese, M. B. H.; Pennycook, S. J.; Venkatesan, T.; Dong, S.; Xue J. M.; Chen, J. Electronic-reconstruction-enhanced hydrogen evolution catalysis in oxide polymorphs. *Nat. Commun.* **2019**, *10*, 3149.
51. Zhao, J.; Li, W.; Wu, S.; Xu, F.; Du, J.; Li, J.; Li, K.; Ren, J. and Zhao, Y. Strong interfacial interaction significantly improving hydrogen evolution reaction performances of MoS_2/Ti_4O_7 composite catalysts. *Electrochim. Acta*. **2020**, *337*, 135850.
52. Shang, X.; Rao, Y.; Lu, S. S.; Dong, B.; Zhang, L. M.; Liu, X. H.; Li, X.; Liu, Y. R.; Chai Y. M. and Liu, C. G. Novel WS_2/WO_3 heterostructured nanosheets as efficient electrocatalyst for hydrogen evolution reaction. *Mater. Chem. Phys.* **2017**, *197*, 123–128.
53. Sharma, L.; Kumar P.; Halder, A. Phase and Vacancy Modulation in Tungsten Oxide: Electrochemical Hydrogen Evolution. *ChemElectroChem.* **2019**, *6*, 3420–3428.
54. Guo, B.; Yu, K.; Li, H.; Song, H.; Zhang, Y.; Lei, X.; Fu, H.; Tan, Y.; Zhu, Z. Hollow Structured Micro/Nano MoS_2 Spheres for High Electrocatalytic Activity Hydrogen Evolution Reaction. *Acs Appl. Mater. Inter.* **2016**, *8*, 5517–5525.
55. Yin, Y.; Han, J. C.; Zhang, Y. M.; Zhang, X. H.; Xu, P.; Yuan, Q.; Samad, L.; Wang, X. J.; Wang, Y.; Zhang, Z. H.; Zhang, P.; Cao, X. Z.; Song, B.; Jin, S. Contributions of Phase, Sulfur Vacancies, and Edges to the Hydrogen Evolution Reaction Catalytic Activity of Porous Molybdenum Disulfide Nanosheets. *J. Am. Chem. Soc*. **2016**, *138*, 7965–7972.
56. Liang, K.; Tabassum, A.; Kothakonda, M.; Zhang, X.; Zhang, R.; Kenney, B.; Koplitz, B. D.; Sun, J.; Naguib, M. Two-dimensional titanium carbonitride MXene as a highly efficient

electrocatalyst for hydrogen evolution reaction. Materials Reports: Energy, **2022**, *2*, 100075.

57. Zhu, Y.; Tahini, H. A.; Hu, Z.; Dai, J.; Chen, Y.; Sun, H.; Zhou, W.; Liu, M.; Smith, S.C.; Wang, H.; Shao, Z. Unusual synergistic effect in layered Ruddlesden- Popper oxide enables ultrafast hydrogen evolution. *Nat. Commun*. **2019**, *10*, 1-9.
58. Zhu, Y.; Zhou, W.; Zhong, Y.; Bu, Y.; Chen, X.; Zhong, Q.; Liu, M.; Shao, Z. A perovskite nanorod as bifunctional electrocatalyst for overall water splitting. *Adv. Energy Mater.* **2017**, *7*, 1602122.
59. Xu, X.; Chen, Y.; Zhou, W.; Zhu, Z.; Su, C.; Liu, M; Shao, Z. A Perovskite Electrocatalyst for Efficient Hydrogen Evolution Reaction. *Adv. Mater*. **2016**, *28*, 6442-6448.
60. Dai, J.; Zhu, Y.; Tahini, H. A.; Lin, Q.; Chen, Y.; Guan, D.; Zhou, C.; Hu, Z.; Lin, H. J.; Chan, T.S.; Chen, C. T. Single-phase perovskite oxide with super-exchange induced atomic-scale synergistic active centers enables ultrafast hydrogen evolution. *Nat. Commun.* **2020**, *11*, 1-10.